Progress In Electromagnetics Research C, Vol. 97, 189–200, 2019

Phase Statistical Model and Correction in Imagery of Ground Based Synthetic Aperture Radar (GBSAR) for Land Deformation Monitoring

Chee-Siong Lim*, Yee-Kit Chan, Voon-Chet Koo, and William How-Hsin Hii

Abstract—There are millions of people in the world exposed to weather-related land deformation hazards. These weather-related mass movement activities are most likely due to climate change, the decrease of permafrost area, the change in precipitation pattern, etc. Landslide is the most common land deformation incidents reported in Malaysia for the past few years. Therefore, Remote Sensing and Surveillance Technologies (CRSST), Multimedia University (MMU), Malaysia has developed the ground-based synthetic aperture radar (GBSAR) as a tool to monitor the high-risk area, which is prone to landslide continuously. Preliminary testing of the GBSAR has been conducted in Cameron Highland, Malaysia to verify the performance of the GBSAR and its capability of detecting landslide. However, the phase stability of the GBSAR is one of the most crucial factors that affect the detection capability of GBSAR, especially when it comes to the sub-mm measurement. This paper reports the phase stability study of the GBSAR and presents an empirical model for interferometric phase statistics.

1. INTRODUCTION

Hazards due to ground movements and instability in human-made structures potentially lead to considerable human and economic losses. Conventional ground and structural movement monitoring systems use geodetic methods such as total stations, levelling, and GPS, which are very limited to observations at distinct points. Laser scanning and photogrammetric techniques, on the other hand, cover wider areas, but they can only be operated during day time and under right weather conditions. With the recent development of interferometric synthetic aperture radar (InSAR), it is possible to monitor the displacements in a large area remotely with high spatial resolution regardless of weather conditions. Many research works have been conducted for ground displacements monitoring such as ground displacements at a regional scale due to subsidence [2], earthquakes and volcanoes [8, 11, 12], landslides [1, 4], and glacier motion [7, 14]. However, most of the InSAR systems are satellite-based and therefore limit the response time of the radar system. Thus, this project aims to utilise a ground-based SAR system for timely remote monitoring earth environments, especially for landslides and terrain subsidence.

2. SYSTEM DESCRIPTION

A GBSAR has been designed and developed by Centre for Remote Sensing & Surveillance Technologies, Multimedia University, Malaysia. The detailed specification of the GBSAR system is listed in Table 1. The functional block diagram of the GBSAR system is shown in Fig. 1(a). It consists of a linear scanning platform, an RF module, antenna system, embedded SAR processor, and some supporting

Received 5 September 2019, Accepted 25 November 2019, Scheduled 11 December 2019
* Corresponding author: Chee-Siong Lim (cslim@mmu.edu.my).
The authors are with the Multimedia University, Malaysia.

Table 1. System parameter of GBSAR.

Design Parameter	Design Value
Operating Frequency	17.2 GHz
Bandwidth	400 MHz
Waveform	FMCW
Polarization	Single
Transmit Power	1 W
Antenna Gain	16 dBi
3 dB beamwidth	20° (azimuth), 20° (elevation)
Synthetic Length	1.5 m
Range Resolution	0.5 m
Azimuth Resolution	5.8 mrad
Maximum Sensing Distance	2000 m
Sigma Naught	−20 dB
SNR	> 10 dB

submodules. The RF module, antenna system, and embedded SAR processor form essential components of the SAR system, whereas the linear scanning platform will act as the moving platform of the SAR system. Fig. 1(b) illustrates the working principle of the GBSAR. It is similar to normal strip map SAR configuration, but the platform is ground-based. The antenna will move along the linear scanning platform to complete the whole synthetic length.

In order to acquire more stable and fine resolution linear movement, a high-precision linear scanning platform has been developed. A CAD drawing of the linear guide system is shown in Fig. 2(a). It consists of a scanning rail of 1.5 meter length. For each of the GBSAR acquisition, the antenna will move along the rail, and a total of 150 range sample points of 10 mm spaced intervals along the azimuthal direction will be captured. The actual hardware implementation is shown in Fig. 2(b). The total weight of the whole linear scanning platform is about 20 kg.

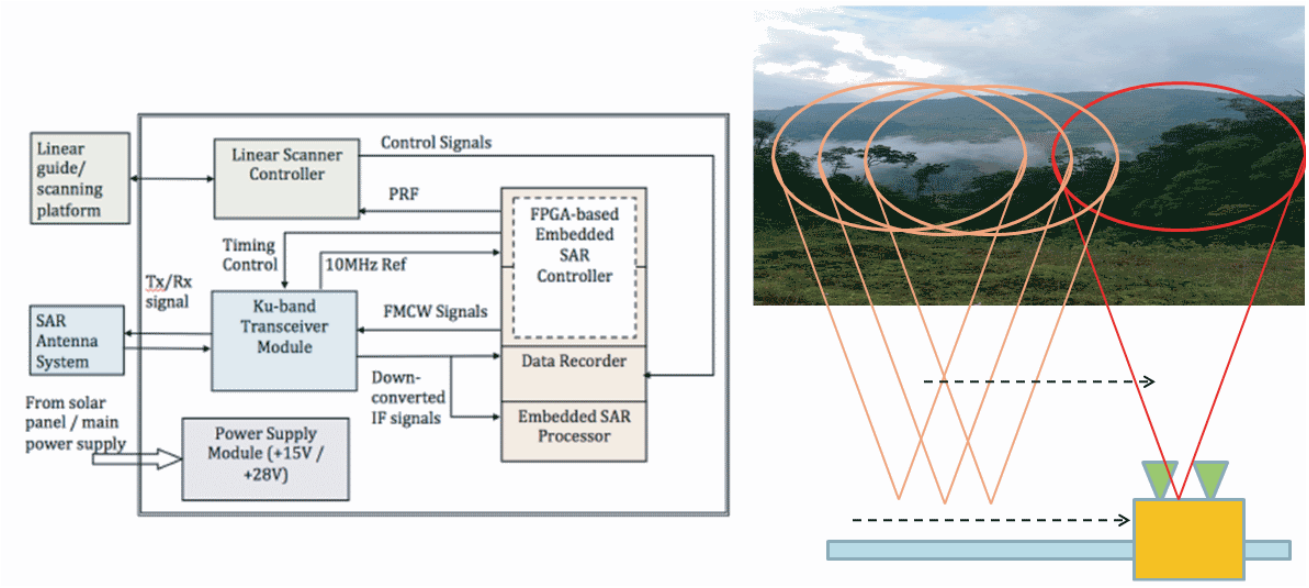

Figure 1. (a) Functional block diagram of GBSAR. (b) Operation principle of GBSAR.

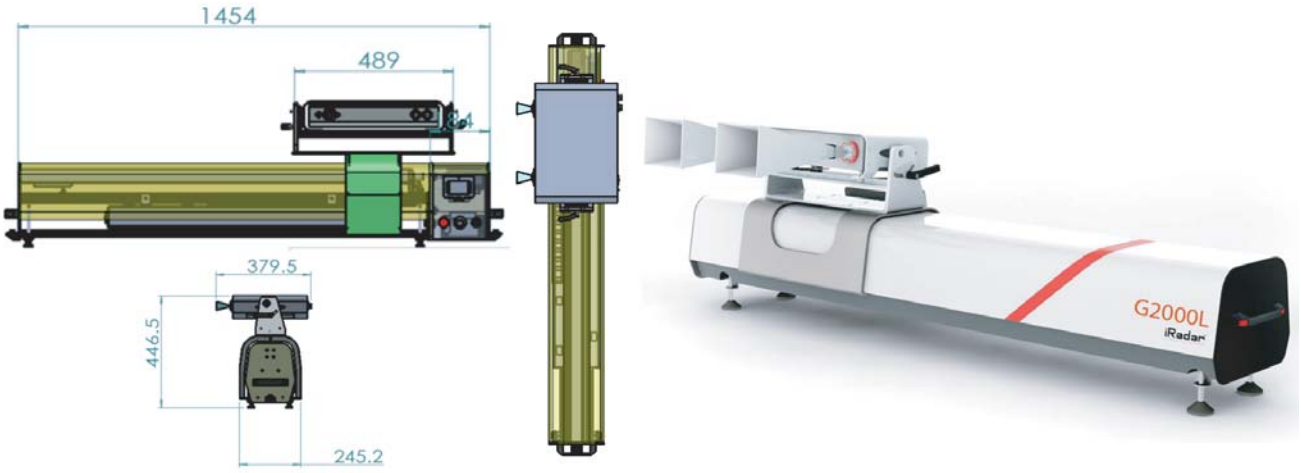

(a) (b)

Figure 2. (a) Design of linear scanning platform, (b) linear scanning platform construction.

3. INTERFEROMETRIC SYNTHETIC APERTURE RADAR (INSAR)

3.1. Introduction

The implementation of interferometry into radar signal processing first appeared in the late 1960s and early 1970s with the observation of Venus and the Moon's surface. In 1974, Graham [5] first introduced interferometric techniques into synthetic aperture radar signal processing. The working principle of the Interferometric Synthetic Aperture Radar (InSAR) covers three primary stages. In stage one, two satellite-borne SAR imaging campaigns are conducted on the same area [10]. Next, the phases in the two SAR images are compared to produce the interferogram. In the final stage, the terrain elevation data are extracted and acquired from the phase information in the interferogram. In 1986, a side-looking airborne SAR system was installed on a NASA CV990 aircraft [13], and transmitted radar signal with one transmitter and received ground echo signal via two receivers simultaneously. In this experiment, they have successfully acquired data at San Francisco, California, USA. Two complex images of the region were processed to generate complex interferograms related to the terrain, and finally, a terrain heightmap with higher resolution was obtained.

The European Space Agency launched the C-band ERS-1 satellite in July 1991, followed by a large number of articles, focusing on the potential applications of InSAR [11]. The launch of the ERS-2 in 1995 made it possible to perform interference processing using images of ERS-1 and ERS-2 one day apart and greatly improved the processing accuracy. At the end of 2000, the Shuttle Radar Topography Mission (SRTM) which was jointly developed by the United States, Germany and Italy was successfully launched. SRTM used dual-antenna radar interferometry to cover nearly 80 percent of the Earth's land surface in its 10-day flight [3]. The elevation measurement accuracy can achieve up to 6 meters. The acquired data can produce 3D integrated terrain information, which can be used for weapon guidance, military mission planning, flight training simulation, and navigation.

3.2. InSAR Processing

The major processes to produce the interferometric SAR images include:

(1) Data acquisition — Collection of Independent SAR data sets
(2) Generation of Complex SAR images
(3) Registration of SAR images
(4) Interferogram generation
(5) Flat earth removal

(6) Phase unwrapping (removes modulo-2π ambiguity)
(7) Height calculation
(8) Geometry conversion and geocoding of Interferometric image

The InSAR processing flowchart is shown in Fig. 3.

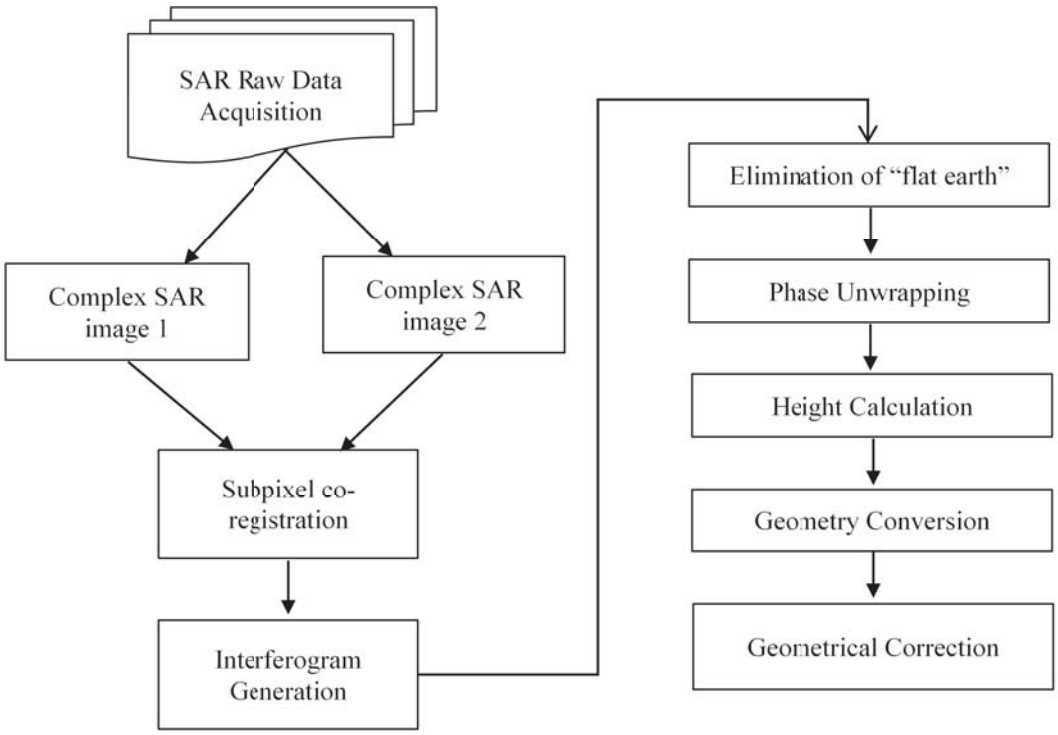

Figure 3. InSAR processing flow chart.

During the step of interferogram generation, two ground-based InSAR complex images after high-precision registration are conjugate multiplied to generate an interference phase map, and the interference phase at this time includes deformation information of the target region.

RF system typically possesses internal noise. This noise will be revealed during the processing of the data, causing the decline in the signal-to-noise (SNR) ratio of the interference phase map and the phase coherency. It affects the subsequent data processing, and consequently, the measurement accuracy of the ground-based InSAR system will be compromised. Therefore, the modelling of the noise in the system is crucial as it can be used to predict the noise present in the measurement. The noise removal process can be performed based on the built model to improve the signal to noise ratio of generated images. The improvement in the SNR leads to better coherency in the interferogram, which will subsequently ease the phase unwrapping process in the following stage. The deformation of the target region will be estimated via the phase unwrapped information. In order to obtain high precision measurement results, the noise estimation and suppression need to be performed.

Generally, InSAR Phase is the sum of several effect. The overall expression of InSAR phase can be written as below,

$$\varphi^w = \varphi_{\text{topo}} + \varphi_{\text{disp}} + \varphi_{\text{atm}} + \varphi_{\text{noise}} - 2\pi n \tag{1}$$

where φ_{topo} is the phase difference due to the topography in the case of a spatial baseline; φ_{disp} is the phase related to the displacement; φ_{atm} is the phase due to atmospheric effects during image acquisition; φ_{noise} represents the phase noise that occurs in the system; and finally the term $2\pi n$ is because the phase is wrapped and bounded in the range $[-\pi, \pi]$ where n is an integer number.

For temporal change detection application, it is assumed that the spatial baseline is zero (i.e., $\varphi_{\text{topo}} = 0$). Therefore, measurement of displacement phase φ_{disp} can be rewritten as,

$$\varphi_{\text{disp}} = \varphi^{w} - \varphi_{\text{atm}} - \varphi_{\text{noise}} + 2\pi n \tag{2}$$

Finally, the line of sight displacement can be calculated via the equation as below,

$$d = \frac{\lambda}{4\pi}\varphi_{\text{disp}} \tag{3}$$

with standard deviation given by

$$\sigma_d = \frac{\lambda}{4\pi}\sigma_{\varphi_{\text{disp}}} \tag{4}$$

3.3. Problem Statement

In order to obtain a precise estimation of displacement, InSAR phase statistical characteristic needs to be analysed to precisely estimate the temporal variation associated with the phase change. A commonly used assumption is to model SAR echoes as a stationary Gaussian process (homogenous scene). This assumption is not valid for the case of a non-homogenous scene or when there are point scatterers under the scene of observation. Probability density function (PDF) of InSAR phase in Homogenous Scene [6] can be expressed as

$$\text{PDF}(\varphi) = \frac{1-|\gamma|^2}{2\pi}\frac{1}{1-\beta^2}\left(1 + \frac{\beta\cos^{-1}(\beta)}{\sqrt{1-\beta^2}}\right) \tag{5}$$

where

$$\beta = |\gamma|\cos(\varphi - \varphi_o) \tag{6}$$

$$\varphi_o = E\{\varphi\} \tag{7}$$

with the coherency defined as:

$$|\gamma| = \left|\frac{E\{Z_1 Z_2^*\}}{\sqrt{E\{|Z_1|^2\}E\{|Z_2|^2\}}}\right|, \quad 0 \le |\gamma| \le 1 \tag{8}$$

where Z_1 and Z_2 are the master and slave SLC data, respectively.

3.4. Experiment Setup for Verification of Phase Statistical Model

An indoor experiment has been set up in an anechoic chamber for continuous scanning of a single point target which is conducted for 18 days with an interval of 1/2 hour per scan. A total of 800 sets of raw data have been collected in this experiment. The setup of the measurement is shown in Fig. 4. The point target (a trihedral, with the side edge of 25 cm) is located at 6.6 m from the GBSAR. Fig. 5 shows the actual setup in the chamber.

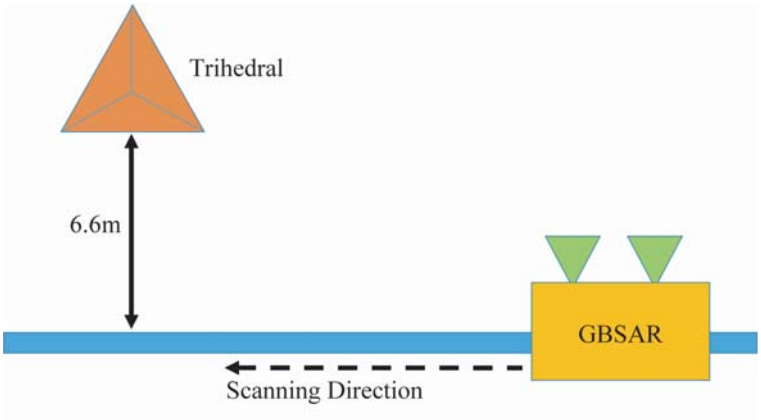

Figure 4. Experimental setup for phase stability.

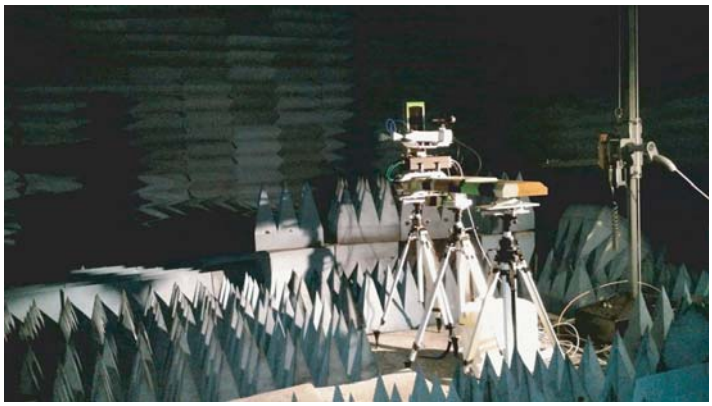

Figure 5. GBSAR measurement in anechoic chamber.

3.5. Measurement Results

SAR data are collected from the 18 days continuous scanning, and a total of 800 sets of SAR images are successfully generated (using the Range Migration Algorithm). Fig. 6 shows one of the sample SAR images generated for the GBSAR indoor experiments. A strong reflection at 6.6 m can be observed which corresponds to the trihedral placed at 6.6 m apart from the GBSAR. The coherency map is generated and shown in Fig. 7(a). The pixel/point with coherency more than 0.9 will be selected for phase stability analysis as they are highly correlated in time (or in respect of time). Fig. 7(b) shows the selection area. It can be observed that most of the points are concentrated around the trihedral corner reflector. A total of 228 points are selected and used for subsequent analysis.

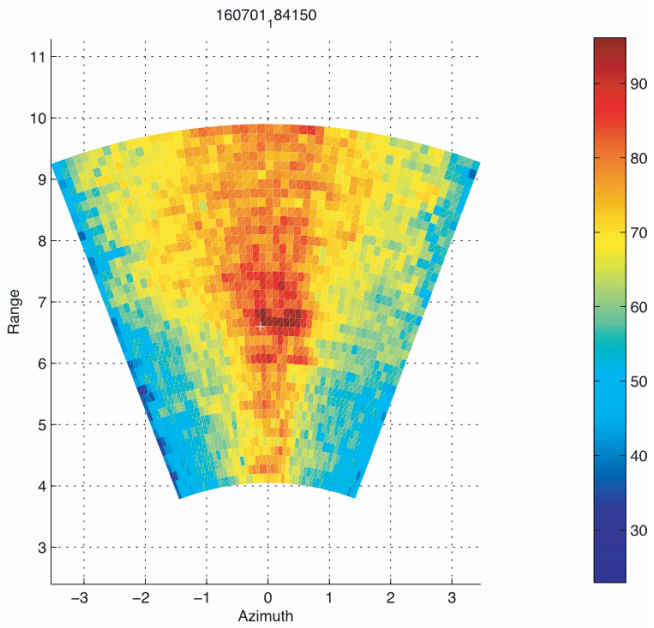

Figure 6. Sample SAR image generated from the experiment.

The displacement variation for 228 points across 18 days or 800 measurements is plotted and shown in Fig. 8. It can be observed that the displacements of the same single point/pixel are varied from −0.3 mm to 0.6 mm across 800 samples over the 18 days. Such displacements are considered as errors since the target of measurement is static. The systematic errors are mainly due to the phase error by the RF module and mechanical error of the linear guide. These errors will be investigated and

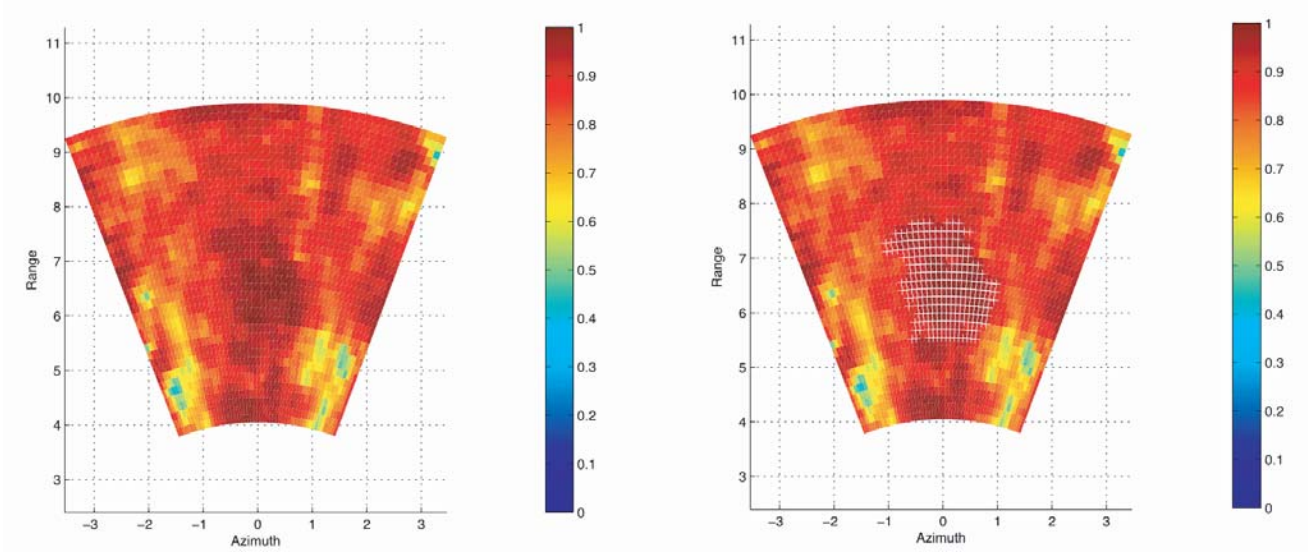

Figure 7. (a) Coherency map generated from average of 800 images. (b) Selection of point with coherency more than 0.9.

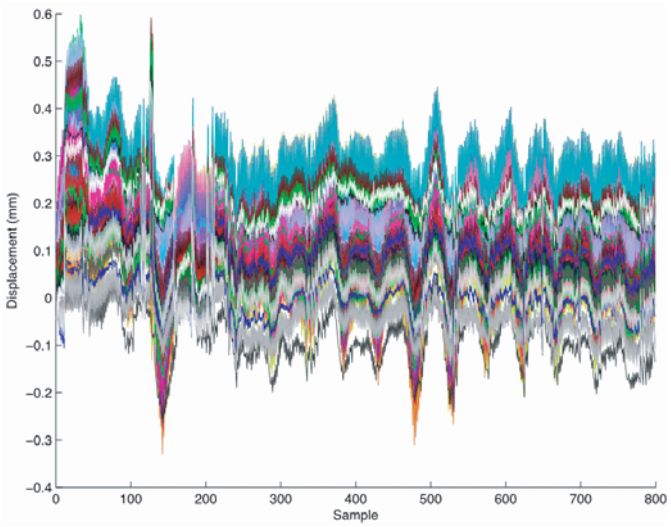

Figure 8. Displacement variation in mm (over 18 days) for 228 points.

reduced to obtain the best displacement estimation of the scanned area.

The single point response is extracted, and it can be observed in Fig. 9(a). By zooming into Fig. 9(a), it can be separated by two responses, i.e., displacements, due to the right scan and left scan. The displacements due to the right scan and left scan are shown in Fig. 9(b).

It is observed that there is a bias error due to the mechanical right and left scans, which amounts to about 0.0975 mm. In order to correct this error, the absolute location for end position for right and left scans is extracted from the linear guide. Fig. 10(a) shows the end position of the right scan, whereas Fig. 10(b) shows the end position of the left scan. The mechanical errors due to different end positions along the scanning period are about ± 0.1 mm. These mechanical errors are then removed from the displacement response for 800 scans, and the resultant output is shown in Fig. 11. The standard deviation is 0.0465 mm after the removal of mechanical errors compared to 0.0673 mm.

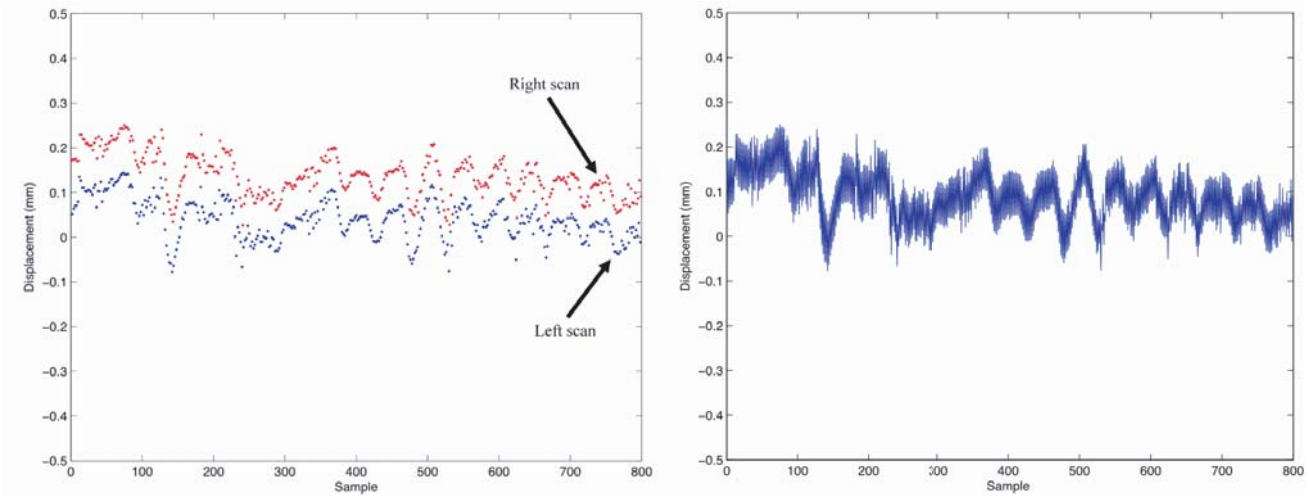

Figure 9. (a) Displacement variation in mm (over 18 days) for single point. (b) Zoom in view.

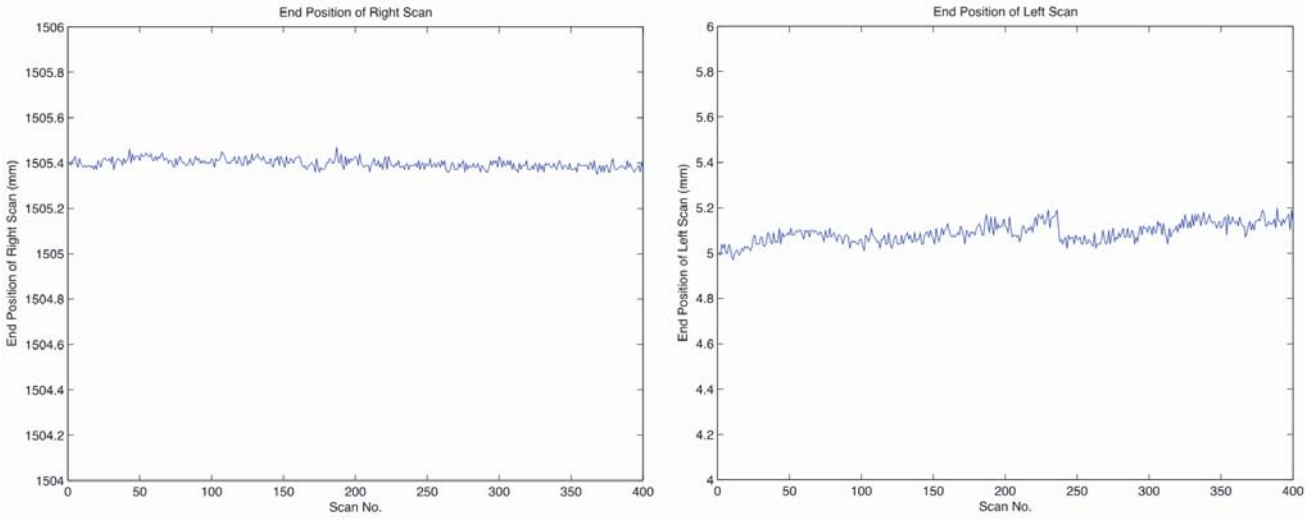

Figure 10. (a) End position (reading from absolute magnetic linear encoder) of right scan for total 400 scans. (b) End position (reading from absolute magnetic linear encoder) of left scan for total 400 scans.

Finally, the distribution of InSAR phase is plotted and displayed in Fig. 12(a). Both distributions with the coherencies of 0.8 and 0.9 are plotted in the same graph. Therefore, the PDF of InSAR phase in Isolated Point Scene for our GBSAR system can be modelled as t-distribution. The PDF for t-distribution can be expressed as below [9].

$$\mathrm{PDF}(\varphi) = \frac{\Gamma\left(\dfrac{v+1}{2}\right)}{\sigma\sqrt{v\pi}\,\Gamma\left(\dfrac{v}{2}\right)}\left[\frac{v+\left(\dfrac{x-\mu}{\sigma}\right)^2}{v}\right]^{-\left(\frac{v+1}{2}\right)} \tag{9}$$

where $\Gamma(\cdot)$ is the gamma function, μ the location parameter (mean), σ the scale parameter, and v the

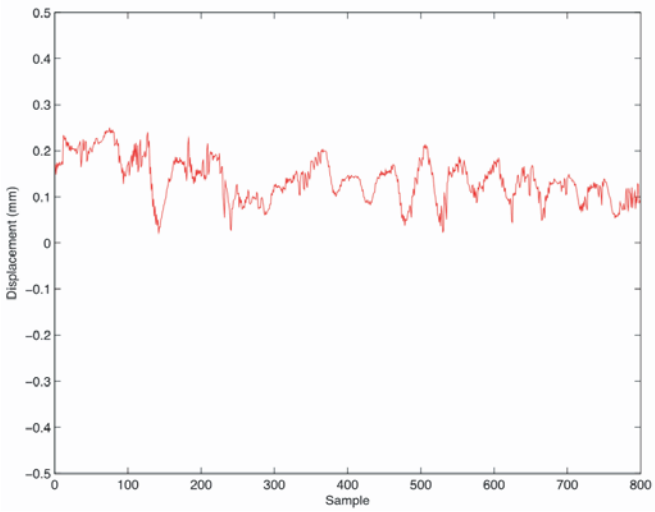

Figure 11. Mechanical bias error removal.

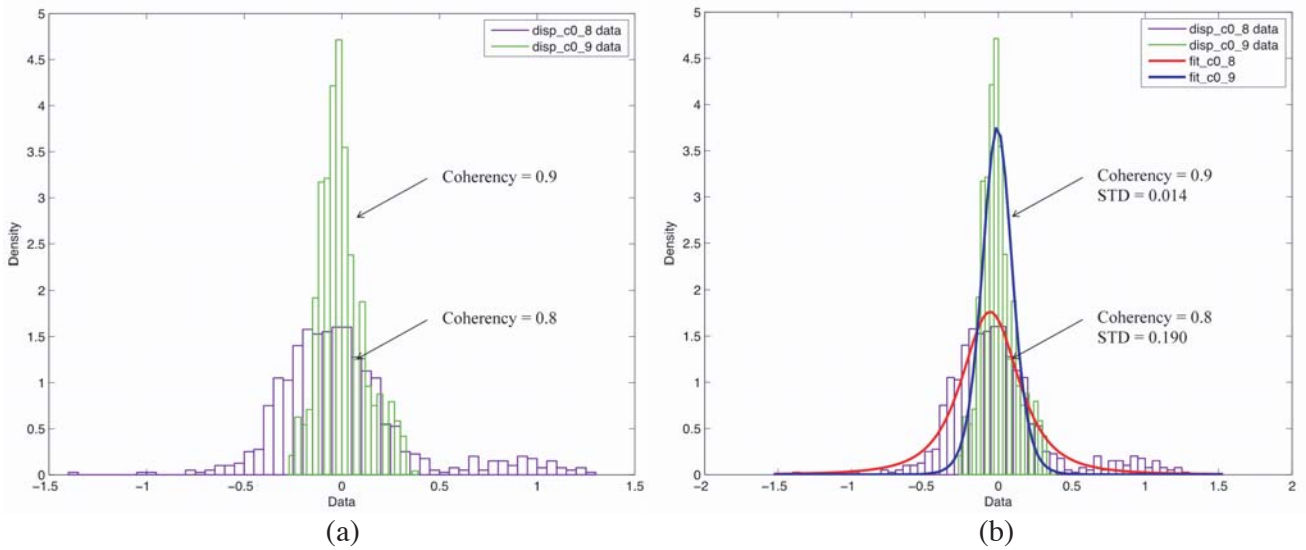

Figure 12. (a) Statistical distribution of InSAR phase. (b) Phase model using t-distribution.

shape parameter.

Figure 12(b) shows the phase model for both coherencies of 0.8 and 0.9 using t-distribution. The standard deviations of the two cases are 0.19 and 0.014, respectively, which indicates that the model used is well matched to the data.

3.6. Field Measurement

Preliminary testing of the GBSAR has been conducted in Cameron Highland, Malaysia to verify the performance of the GBSAR and the capability of landslide detection. A photo of the test site is shown in Fig. 13(a), and an external artificial target (trihedral, shown in Fig. 13(b) is used to confirm the correct detection of the test site. Two trihedrons have been used in the experiment. The distance from GBSAR to two trihedrons are about 1244 m and 1259 m, respectively. The contour of the test site is shown in Fig. 14.

Besides the phase errors due to the mechanical bias error, the atmospheric conditions may introduce

(a) (b)

Figure 13. (a) Field measurement test site at Cameron Highland, Malaysia. (b) Trihedral corner reflector as external target.

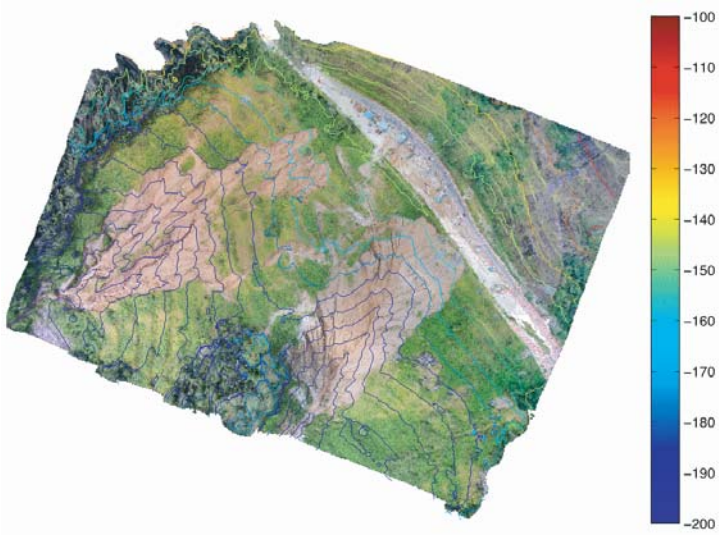

Figure 14. Study area TS01: Gunung Pass, Malaysia.

a significant amount of phase noise to the return echo as well. We can model the phase noise as a normal distribution, while the atmospheric effects are contributed by two major components, i.e., dry component and wet component. The expression of the phase due to the atmospheric effect can be shown as below.

$$\varphi_{\text{atm}} = \{\text{dry component}\} + \{\text{wet component}\} \tag{10}$$

$$\varphi_{\text{atm}} = \frac{4\pi}{\lambda}\left(7.76 \times 10^{-5}\int_0^r \frac{P}{T}dr + 0.373\int_0^r \frac{e}{T^2}dr\right) \tag{11}$$

where P is the atmospheric pressure in hPa, T the temperature in Kelvin, e the partial pressure of the water vapour in hPa, and r the distance between target and instrument [15].

Figure 15 shows the SAR image generated with marker indicating the location of the one of the corner reflector which coincides with the measurement setup described above. Fig. 15(a) shows the first target at 1268.10 m from the GBSAR, whereas Fig. 15(b) shows the second target at 1253.25 m.

In order to verify the capability of GBSAR for deformation detection, the trihedral corner reflector is adjusted with a 0.5 mm step to simulate the changes of the terrain. A series of scanning is performed with different step sizes of trihedral. The displacement information of the trihedral is extracted from the phase change of the target in the SAR images. The extracted phase is corrected by removing the

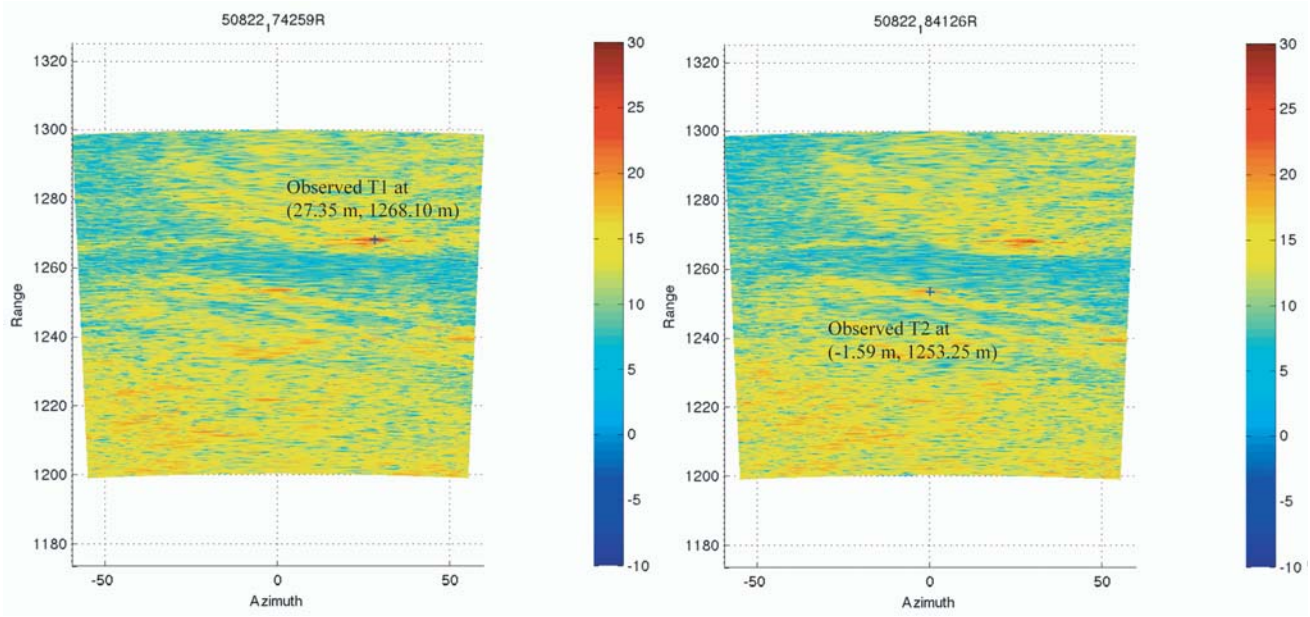

(a) (b)

Figure 15. SAR images generated with highlighted targets.

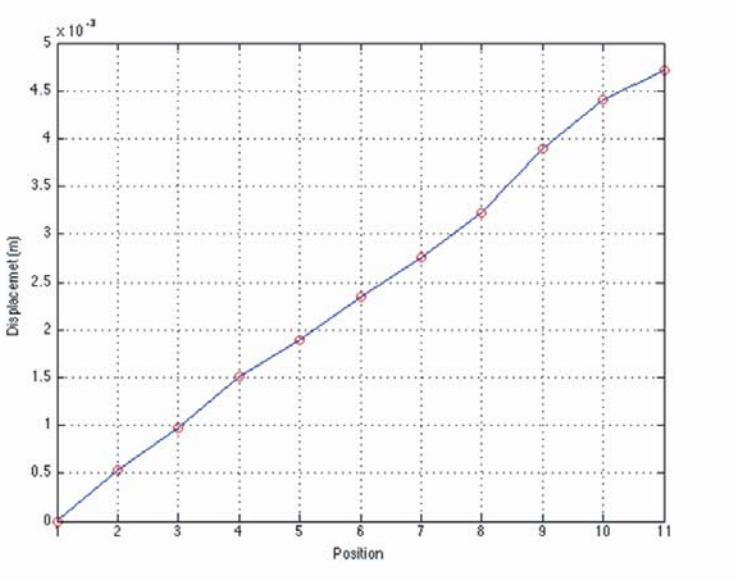

Figure 16. Measured displacement of 0.5 mm per step.

phase errors due to mechanical misalignment and predicted phase noise using t-distribution.

The measurement result is shown in Fig. 16. The y-axis corresponds to the measured displacement based on the phase change of the received signal, and x-axis corresponds to the displacement position of the trihedral in which each position is equivalent to 0.5 mm of changes.

4. CONCLUSION

The InSAR phase statistics of a non-homogenous scene have been studied. It is observed that t-distribution fits well in the case of an isolated point scene. The phase errors due to various factors

have been taken into account, and phase errors correction has been performed to improve the phase quality. The performance of the GBSAR is verified by a series of outdoor field experiments, with change detection capability of 0.5 mm. The GBSAR is currently used for the land deformation study and landslide monitoring in Malaysia.

ACKNOWLEDGMENT

The authors would like to thank iRadar Sdn. Bhd. for their collaboration in the realisation of the ground based synthetic aperture radar (GBSAR) project for land deformation monitoring.

REFERENCES

1. Crosetto, M., B. Crippa, and E. Biescas, "Early detection and in-depth analysis of deformation phenomena by radar interferometry," *Engineering Geology*, Vol. 79, Nos. 1–2, 81–91, 2005.
2. Ferretti, A., A. Monti-Guarnieri, C. Prati, F. Rocca, and D. Massonet, *InSAR Principles-guidelines for SAR Interferometry Processing and Interpretation*, TM-19, ESA Publications, The Netherlands, 2007.
3. Gens, R. and J. L. van Genderen, "Review article sar interferometry — Issues, techniques, applications," *International Journal of Remote Sensing*, Vol. 17, No. 10, 1803–1835, 1996.
4. Goldstein, R. M., H. Engelhardt, B. Kamb, and R. M. Frolich, "Satellite radar interferometry for monitoring ice sheet motion: Application to an antarctic ice stream," *Science*, Vol. 262, No. 5139, 1525–1530, 1993.
5. Graham, L. C., "Synthetic interferometer radar for topographic mapping," *Proceedings of the IEEE*, Vol. 62, No. 6, 763–768, 1974.
6. Just, D. and R. Bamler, "Phase statistics of interferograms with applications to synthetic aperture radar," *Applied Optics*, Vol. 33, No. 20, 4361–4368, 1994.
7. Kenyi, L. W. and V. Kaufmann, "Estimation of rock glacier surface deformation using sar interferometry data," *IEEE Transactions on Geoscience and Remote Sensing*, Vol. 41, No. 6, 1512–1515, 2003.
8. Lanari, R., O. Mora, M. Manunta, J. J. Mallorquí, P. Berardino, and E. Sansosti, "A small-baseline approach for investigating deformations on full-resolution differential sar interferograms," *IEEE Transactions on Geoscience and Remote Sensing*, Vol. 42, No. 7, 1377–1386, 2004.
9. Lange, K. L., R. J. A. Little, and J. M. G. Taylor, "Robust statistical modeling using the T distribution," *Journal of the American Statistical Association*, Vol. 84, No. 408, 881–896, 1989.
10. Lazarov, A., C. Minchev, and D. Minchev, "Multi-satellite interferometric SAR system," *Proceedings of the Fifth International Conference on Telecommunications and Remote Sensing — Volume 1: ICTRS*, 33–42, INSTICC, SciTePress, 2016.
11. Massonnet, D. and T. Rabaute, "Radar interferometry: Limits and potential," *IEEE Transactions on Geoscience and Remote Sensing*, Vol. 31, No. 2, 455–464, 1993.
12. Yun, S.-H., *Volcano Deformation Modeling Using Radar Interferometry*, VDM Verlag Dr. Müller, 2008.
13. Zebker, H. A. and R. M. Goldstein, "Topographic mapping from interferometric synthetic aperture radar observations," *Journal of Geophysical Research: Solid Earth*, Vol. 91, No. B5, 4993–4999, 1986.
14. Zebker, H. A., P. A. Rosen, R. M. Goldstein, A. Gabriel, and C. L. Werner, "On the derivation of coseismic displacement fields using differential radar interferometry: The landers earthquake," *Journal of Geophysical Research: Solid Earth*, Vol. 99, No. B10, 19617–19634, 1994.
15. Zebker, H. A., P. A. Rosen, and S. Hensley, "Atmospheric effects in interferometric synthetic aperture radar surface deformation and topographic maps," *Journal of Geophysical Research: Solid Earth*, Vol. 102, No. B4, 7547–7563, 1997.